

Probing vacuum birefringence in an Ultrastrong Laser Field via High-energy Gamma-ray Polarimetry

Da-Lin Wang^a, Xian-Zhang Wu^a, Rui-Qi Qin^a, Jiang-Tao Han^b, Peng-Pei Xie^a, Bing-Jun Li^{a,*}, Huai-Hang Song^c, Yan-Fei Li^{a,**}

^aSchool of Energy and Power Engineering, Xi'an Jiaotong University, Xi'an, 710049, China

^bInstitute of Nuclear and New Energy Technology, Tsinghua University, Beijing, 100084, China

^cLaboratory of Zhongyuan Light, School of Physics, Zhengzhou University, Zhengzhou, 450001, China

Abstract

Vacuum birefringence (VB), a fundamental prediction of nonlinear QED, has eluded direct laboratory detection due to its extreme weakness. We propose a compact, “self-probing” scheme where a GeV electron beam collides head-on with a petawatt laser pulse. Circularly polarized γ -ray photons, generated via nonlinear Compton scattering in the same pulse, then probe the birefringent vacuum it induces. This integrated design bypasses the stringent synchronization and beam transport requirements of traditional pump-probe setups. Our nonperturbative strong-field QED simulations reveal a clear VB signature: conversion of circular to linear polarization, with the induced Stokes parameter S_1 reaching ~ 0.019 within the selected angular range. This corresponds to a refractive index difference $\Delta n = 1.829 \times 10^{-4}$ over micron-scale paths, directly measurable as a high-contrast “X-shape” asymmetry in e^+e^- pair distributions. The scheme provides a feasible path to first laboratory VB detection with current laser and accelerator technologies.

Keywords: vacuum birefringence, nonlinear Compton scattering, photon polarization

1. Introduction

Vacuum birefringence (VB), a phenomenon where the quantum vacuum acquires different refractive indices for distinct light polarizations in a strong field, is a fundamental prediction of nonlinear quantum electrodynamics (QED). It originates from vacuum polarization (VP), the transient fluctuation of virtual electron-positron pairs induced by an intense electromagnetic background [1, 2, 3]. While theoretically well-established, the experimental detection of VB remains a major challenge. The effect is governed by the quantum nonlinearity parameter χ_γ and is exceedingly weak at field strengths achievable in laboratories, which are far below the critical Schwinger field ($E_{\text{cr}} \approx 1.3 \times 10^{18}$ V/m). Consequently, amplifying the feeble VB signal to a measurable level demands innovative experimental strategies.

A common strategy in these attempts has been the pump-probe architecture, which employs separate systems to generate the strong field and to produce or probe the photons. These approaches can be categorized by the probe photon energy. First, optical-wavelength experiments such as PVLAS and BMV employ high-finesse cavities and static magnetic fields to achieve extraordinary sensitivity [4, 5, 6]. Despite their high sensitivity, they are fundamentally limited by the low photon energy and

weak field strength, struggling to overcome noise over long beam paths. Second, schemes utilizing X-ray probes, exemplified by the HIBEF project at European XFEL [7, 8, 9, 10, 11], exploit the shorter wavelength to enhance the effect per photon. Here, the principal technical hurdles become the femtosecond- and micrometer-level synchronization of two independent light sources and the preservation of polarization fidelity through X-ray optics. Third, theoretical designs using GeV γ -rays aim to further boost the signal by maximizing the quantum parameter χ_γ [12, 13, 14, 15, 16]. They typically involve a complex three-beam setup (electron-laser collision for photon generation plus a separate laser for probing), which inherits the major synchronization and alignment challenges of the pump-probe architecture.

Notably, while many of these proposals were statistically viable in principle, their practical implementation has been hindered by cumulative technical hurdles—including femtosecond-level synchronization between independent beams, signal degradation during probe-beam transport, and vulnerability to spatiotemporal jitter and unforeseen systematic noises. This recurring pattern underscores the value of an architecture that intrinsically minimizes such implementation complexities.

In parallel, observational evidence suggestive of vacuum birefringence has emerged from extreme astrophysical environments. Measurements of polarized optical emission from isolated neutron stars [17, 18] show signatures consistent with VB predictions in ultra-strong magnetic fields. Similarly, recent analyses of polarized $\gamma\gamma \rightarrow e^+e^-$ processes in ultra-peripheral heavy-ion collisions, such as those reported by the STAR collaboration [19], reveal azimuthal asymmetries interpretable as arising from birefringence-like effects where the

*Corresponding author

**Principle Corresponding author

Email addresses: wangdalin133@stu.xjtu.edu.cn (Da-Lin Wang), 3123303391@stu.xjtu.edu.cn (Xian-Zhang Wu), qrq2833757055@stu.xjtu.edu.cn (Rui-Qi Qin), hanjt25@mails.tsinghua.edu.cn (Jiang-Tao Han), xiepengpei@stu.xjtu.edu.cn (Peng-Pei Xie), lbj_xjtu@stu.xjtu.edu.cn (Bing-Jun Li), huaihongsong@gmail.com (Huai-Hang Song), liyanfei@xjtu.edu.cn (Yan-Fei Li)

same electromagnetic field both produces the probing photons and modifies their propagation.

These observations are significant for two reasons. They not only provide indirect yet compelling motivation for VB in nature but also exemplify a unified scenario where photon generation and strong-field interaction are intrinsically co-located—in stark contrast to the separated-beam paradigm of conventional laboratory setups. A controlled laboratory detection of VB would therefore serve a dual purpose: confirming a fundamental QED prediction and establishing a crucial benchmark for interpreting astrophysical and heavy-ion signatures.

To bridge this gap, we propose a compact, integrated scheme that adopts the unified philosophy observed in nature while operating under well-controlled laboratory conditions. As illustrated in Figure 1, a relativistic electron beam collides head-on with an ultrastrong laser pulse. Crucially, the *same* laser field serves a dual role: it generates multi-GeV, circularly polarized γ -photons via nonlinear Compton scattering and simultaneously provides the birefringent medium through which these photons propagate. This “self-probing” architecture inherently guarantees perfect spatiotemporal overlap and eliminates the synchronization and beam-transport complexities that challenge conventional pump-probe experiments.

In this Letter, we demonstrate through comprehensive Monte Carlo simulations that this self-probing scheme induces a clear VB signature. Using a longitudinally polarized, 3 GeV electron beam colliding with a petawatt-class laser pulse ($a_0 = 125$), we observe an average refractive index difference of $\Delta n \approx 1.829 \times 10^{-4}$ for selected photons, accumulating a phase delay of $\Delta\phi \approx 2.343 \times 10^{-2}$ rad over micron-scale paths. This large phase shift, enhanced by the γ -photon’s short wavelength, offers a promising route for the first laboratory observation of VB, with a signal enhanced by nearly 10 orders of magnitude compared to traditional optical experiments.

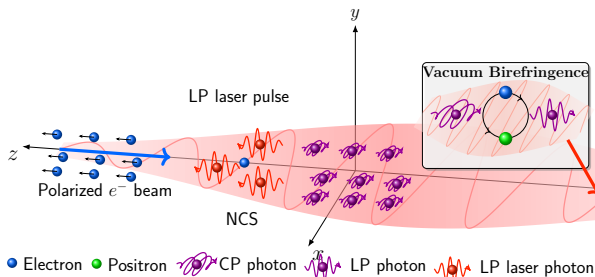


Figure 1: Schematic of the simulation setup. A longitudinally polarized electron beam collides head-on with a high-intensity, linearly polarized laser pulse. The interaction generates high-energy γ -photons that are initially predominantly circularly polarized (large Stokes parameter S_2). As these photons propagate through the remaining laser field, vacuum birefringence (VB) induces a phase difference between polarization components parallel and perpendicular to the laser’s electric field. This causes the photons’ polarization state to evolve from circular toward elliptical, manifesting as a decrease in S_2 and the appearance of a measurable linear polarization component (S_1). The evolution of the Stokes parameters (S_1, S_2, S_3) fully captures this polarization transformation.

2. Simulation Method and Setup

Our scheme operates in the non-perturbative regime where the quantum nonlinearity parameter for photons, χ_γ , approaches unity ($\chi_\gamma \sim 1$). For a high-energy photon in a head-on collision with an intense laser field, χ_γ is given by

$$\chi_\gamma \approx 0.5741 \frac{\omega_\gamma}{\text{GeV}} \sqrt{\frac{I}{10^{22} \text{ W/cm}^2}}, \quad (1)$$

where ω_γ is the photon energy and I is the laser intensity. This parameter is boosted to $\chi_\gamma \sim 1$ by the counter-propagating geometry and the GeV-scale photon energy, placing the interaction firmly in the regime where non-perturbative strong-field QED effects dominate. In this regime, we adopt the theoretical framework of Bragin et al. [13], where the vacuum’s refractive and absorptive properties are treated via the full polarization operator. This formalism maps quantum vacuum effects onto an evolution of the photon’s Stokes vector: VB manifests as a phase-induced conversion between linear and circular polarization states.

2.1. Numerical Framework and Implementation

The simulations are performed using a Monte Carlo method that incorporates all polarization effects [20, 21, 22], including vacuum birefringence (VB) and vacuum dichroism (VD), based on the local constant field approximation (LCFA) [23, 24, 25, 26, 27]. Quantum probabilities, derived via the Baier–Katkov QED operator method within the LCFA, are employed throughout.

The electron trajectories are computed using a fourth-order Runge–Kutta method, ensuring accurate propagation in the ultrastrong laser field. The laser field is modeled as a focused Gaussian pulse with a nonparaxial profile that includes corrections up to order $(w_0/z_r)^3$, where w_0 is the beam waist and z_r the Rayleigh length [28].

At each time step, the electron (or positron) Stokes polarization vector ζ_p evolves into ζ_f^R after photon emission. Here ζ_p (ζ_f^R) denotes the electron spin polarization vector in a mixed state before (after) radiation, expressed in the electron rest frame. If no photon is emitted during the step, the electron spin evolves into ζ_f^{NR} according to the no-emission probability, which originates from the one-loop contribution to the electron mass operator.

Spin precession between emission events is governed by the Thomas–Bargmann–Michel–Telegdi (TBMT) equation, including the field-dependent anomalous magnetic moment from one-loop vertex corrections [29, 30, 31, 32]. Between quantum events, the electron (or positron) dynamics in the laser field are described classically by the Lorentz equation. The Stokes vector of a newly created photon or electron–positron pair is determined by the polarization-resolved photon-emission or pair-production probability.

Photon polarization at emission

The polarization state of a newly emitted photon is obtained from the polarization-resolved probability of nonlinear Compton

scattering. Within the LCFA, the differential emission probability reads [20]

$$\frac{d^2 W_{fi}}{du d\eta} = \frac{W_R}{2} (F_0 + S_1 F_1 + S_2 F_2 + S_3 F_3), \quad (2)$$

where

$$W_R = \frac{\alpha m}{8 \sqrt{3} \pi \lambda_c (k \cdot p_i) (1+u)^3}, \quad u = \frac{\omega_\gamma}{\varepsilon_i - \omega_\gamma}.$$

Here ε_i is the electron energy before radiation, $\alpha = 1/137$ the fine-structure constant, λ_c the Compton wavelength, $\eta = k \cdot r$ the laser phase, and p_i, k, r are the four-vectors of the electron momentum before radiation, the laser wave vector, and the coordinate, respectively. The photon Stokes parameters S_1, S_2, S_3 follow the convention of Ref. [13]: S_2 denotes circular polarization (helicity), whereas S_1 and S_3 represent linear polarization with S_3 defined along the laser's x -axis.

The mean Stokes parameters of the emitted photon are given by

$$S_1 = \frac{F_1}{F_0}, \quad S_2 = \frac{F_2}{F_0}, \quad S_3 = \frac{F_3}{F_0}. \quad (3)$$

The functions F_0, F_1, F_2, F_3 are obtained after summing over final electron polarizations:

$$F_0 = \frac{\alpha m^2}{\sqrt{3} \pi \varepsilon_i} \frac{du}{(1+u)^3} \left\{ -(1+u) \int_{\frac{2u}{3\chi_e}}^{\infty} dx K_{1/3}(x) + 2 \left(1+u + \frac{u^2}{2} \right) K_{2/3} \left(\frac{2u}{3\chi_e} \right) - u (\zeta_i \cdot \hat{e}_2) K_{1/3} \left(\frac{2u}{3\chi_e} \right) \right\}, \quad (4)$$

$$F_1 = \frac{\alpha m^2}{\sqrt{3} \pi \varepsilon_i} \frac{du}{(1+u)^3} \left\{ (1+u) K_{2/3} \left(\frac{2u}{3\chi_e} \right) - u \left(1 + u (\zeta_i \cdot \hat{e}_2) K_{1/3} \left(\frac{2u}{3\chi_e} \right) \right) \right\}, \quad (5)$$

$$F_2 = -\frac{\alpha m^2}{\sqrt{3} \pi \varepsilon_i} \frac{du}{(1+u)^3} \left\{ (\zeta_i \cdot \hat{e}_v) \int_{\frac{2u}{3\chi_e}}^{\infty} dx K_{1/3}(x) - \left(2 + u \right) u K_{2/3} \left(\frac{2u}{3\chi_e} \right) \right\}, \quad (6)$$

$$F_3 = \frac{\alpha m^2}{\sqrt{3} \pi \varepsilon_i} \frac{du}{(1+u)^3} \left\{ (1+u) K_{2/3} \left(\frac{2u}{3\chi_e} \right) - u \left(1 + u (\zeta_i \cdot \hat{e}_2) K_{1/3} \left(\frac{2u}{3\chi_e} \right) \right) \right\}, \quad (7)$$

where \hat{e}_v is the unit vector along the electron velocity, \hat{e}_1 the unit vector along the electron acceleration (which, for our counter-propagating geometry with laser polarization along x , aligns with the x -axis), and $\hat{e}_2 = \hat{e}_v \times \hat{e}_1$. In the expressions above, χ_e is the electron quantum strong-field parameter, ε_i the electron energy before emission, and K_ν denotes the modified Bessel function of the second kind of order ν .

In the present work the electron beam is initially fully longitudinally polarized, i.e. $\zeta_i = (0, 0, 1)$. For this configuration the velocity is along the $-z$ -axis and the acceleration (hence the major axis of the polarization ellipse) is along the x -axis, leading to

$$\zeta_i \cdot \hat{e}_v = -1, \quad \zeta_i \cdot \hat{e}_2 = 0.$$

Consequently the general expressions simplify and the initial Stokes parameters of the emitted photon, denoted as $\mathbf{S}^i = (S_1^i, S_2^i, S_3^i)$, become

$$S_1^i = 0, \quad (8)$$

$$S_2^i = \frac{\int_{\frac{2u}{3\chi_e}}^{\infty} dx K_{1/3}(x) + (2+u)u K_{2/3} \left(\frac{2u}{3\chi_e} \right)}{-(1+u) \int_{\frac{2u}{3\chi_e}}^{\infty} dx K_{1/3}(x) + 2 \left(1+u + \frac{u^2}{2} \right) K_{2/3} \left(\frac{2u}{3\chi_e} \right)}, \quad (9)$$

$$S_3^i = \frac{(1+u) K_{2/3} \left(\frac{2u}{3\chi_e} \right)}{-(1+u) \int_{\frac{2u}{3\chi_e}}^{\infty} dx K_{1/3}(x) + 2 \left(1+u + \frac{u^2}{2} \right) K_{2/3} \left(\frac{2u}{3\chi_e} \right)}. \quad (10)$$

2.2. Polarization Evolution Implementation

As photons propagate through the ultrastrong laser field, their polarization state evolves due to VP effects. For a photon with an initial Stokes vector $\mathbf{S}^i = (S_1^i, S_2^i, S_3^i)$, the VB and VD modify its polarization during propagation.

Vacuum birefringence

The VB effect is implemented within the LCFA framework following the formulation of Bragin et al. [13]. The VB-induced rotation in the (S_1, S_2) plane yields the final Stokes components

$$\begin{pmatrix} S_1^f \\ S_2^f \end{pmatrix} = \begin{pmatrix} \cos \delta\phi & -\sin \delta\phi \\ \sin \delta\phi & \cos \delta\phi \end{pmatrix} \begin{pmatrix} S_1^i \\ S_2^i \end{pmatrix}, \quad (11)$$

while the S_3 component remains unchanged under VB. Here $\delta\phi = \phi_1 - \phi_2$ is the accumulated phase difference between the two polarization eigenmodes, computed from

$$\phi_i = -\frac{1}{2kq} \text{Re} [p_i(\chi_\gamma)] \Delta\eta, \quad (12)$$

with

$$\begin{bmatrix} p_1(\chi_\gamma) \\ p_2(\chi_\gamma) \end{bmatrix} = \frac{\alpha m^2}{3\pi} \int_{-1}^{+1} dv \begin{bmatrix} w-1 \\ w+2 \end{bmatrix} \frac{f'(u)}{u}, \quad (13)$$

$w = 4/(1-v^2)$, $u = [w/\chi_\gamma]^{2/3}$, $f(u) = \pi[\text{Gi}(u) + i\text{Ai}(u)]$, and $\eta = \omega_0 t - k_0 z$ being the laser phase.

Vacuum dichroism

The VD effect, which corresponds to polarization-dependent attenuation of photons via the imaginary part of the VP loop, is implemented through a no-pair-production evolution as described in Ref. [22]. At each time step, for a photon with current Stokes vector \mathbf{S}^i , the loop probability is given by

$$W_{\text{loop}} = F_0^L + \mathbf{S}^i \cdot \mathbf{F}^L, \quad (14)$$

where

$$F_0^L = \frac{1}{2} \left\{ 1 - \int_0^1 dx C_p \left[\left(\frac{x}{1-x} + \frac{1-x}{x} \right) K_{2/3}(\rho) + \int_\rho^\infty dx K_{1/3}(x) - S_3^i K_{2/3}(\rho) \right] \Delta t \right\}, \quad (15)$$

$$\mathbf{F}^L = \frac{1}{2} \mathbf{S}^i \left\{ \mathbf{S}^i \left[1 - \int_0^1 dx C_p \left(\int_\rho^\infty dx K_{1/3}(x) + \left(\frac{x}{1-x} + \frac{1-x}{x} \right) K_{2/3}(\rho) \right) \Delta t \right] \right\}. \quad (16)$$

Here $C_p = \alpha m^2 / (\sqrt{3} \pi \omega_\gamma)$, $\rho = 2 / [3 \chi_\gamma x (1-x)]$, and $K_{2/3}$, $K_{1/3}$ are the modified Bessel functions of the second kind. The Stokes vector after the time step, $\mathbf{S}^f = (S_1^f, S_2^f, S_3^f)$, is then obtained as

$$\mathbf{S}^f = \frac{\mathbf{F}^L}{F_0^L}. \quad (17)$$

This treatment accounts for the differential absorption of photons depending on their polarization states, which ultimately leads to a net polarization enhancement. To simplify the equation, we can also write the evolution of the Stokes parameters in a differential form as follows[33]:

$$\frac{dS_1}{dt} = - \int \frac{\alpha m^2 d\varepsilon}{\sqrt{3} \pi \omega_\gamma^2} S_3 S_1 K_{\frac{2}{3}}(\rho), \quad (18)$$

$$\frac{dS_2}{dt} = - \int \frac{\alpha m^2 d\varepsilon}{\sqrt{3} \pi \omega_\gamma^2} S_3 S_2 K_{\frac{2}{3}}(\rho), \quad (19)$$

$$\frac{dS_3}{dt} = \int \frac{\alpha m^2 d\varepsilon}{\sqrt{3} \pi \omega_\gamma^2} (1 - S_3^2) K_{\frac{2}{3}}(\rho), \quad (20)$$

2.3. Simulation Parameters (Baseline)

Unless stated otherwise, all simulations presented in this work employ the following baseline parameters.

The electron beam propagates along $-z$ and contains $N_e = 10^6$ macro-particles. It has a cylindrical profile with a longitudinal length $L_e = 3 \mu\text{m}$ and transverse Gaussian widths $\sigma_{x,y} = 0.3 \mu\text{m}$. The initial mean energy is $\varepsilon_i = 3 \text{ GeV}$, with a 10% (FWHM) energy spread and a 3 mrad (FWHM) angular divergence. The beam is initially fully longitudinally polarized: $\zeta_i = (0, 0, 1)$. These parameters are well within the capabilities of current laser-wakefield accelerators [34].

The laser pulse propagates along $+z$ and is linearly polarized along the x -axis. Its parameters are: wavelength $\lambda_0 = 1 \mu\text{m}$, focal spot size $w_0 = 5 \mu\text{m}$, and duration $\tau = 20 T_0$, where $T_0 = 2\pi/\omega_0$ is the optical period. The peak intensity reaches $I_0 \approx 2.16 \times 10^{22} \text{ W/cm}^2$, corresponding to a normalized vector potential $a_0 = eE_0/(m_e c \omega_0) = 125$. The laser parameters are chosen to be compatible with the capabilities of near-future petawatt-class laser systems [35]. For this baseline configuration, the electron quantum strong-field parameter is

$$\chi_e = \frac{2\gamma a_0 \hbar \omega_0}{m_e c^2} \approx 3.6,$$

where $\gamma = \varepsilon_i/(m_e c^2) \approx 5870$ is the electron Lorentz factor. This places the interaction well into the non-perturbative QED regime ($\chi_e \gtrsim 1$). For a representative high-energy photon of $\omega_\gamma = 1 \text{ GeV}$, the corresponding photon quantum parameter is

$$\chi_\gamma = \frac{\omega_\gamma}{m_e c^2} \frac{2a_0 \hbar \omega_0}{m_e c^2} \approx 1.2,$$

indicating that both electrons and high-energy photons experience significant strong-field QED effects. Any deviations from this baseline parameter set are explicitly noted in the respective sections.

3. Simulation Results

3.1. Angular Selection and Polarization Signatures

Figure 2 presents the angular distributions of key photon properties obtained from our Monte Carlo simulation. A clear correlation between photon energy, emission angle, and polarization state is evident, which we exploit to isolate the high-energy photon population that carries the strongest VB signal.

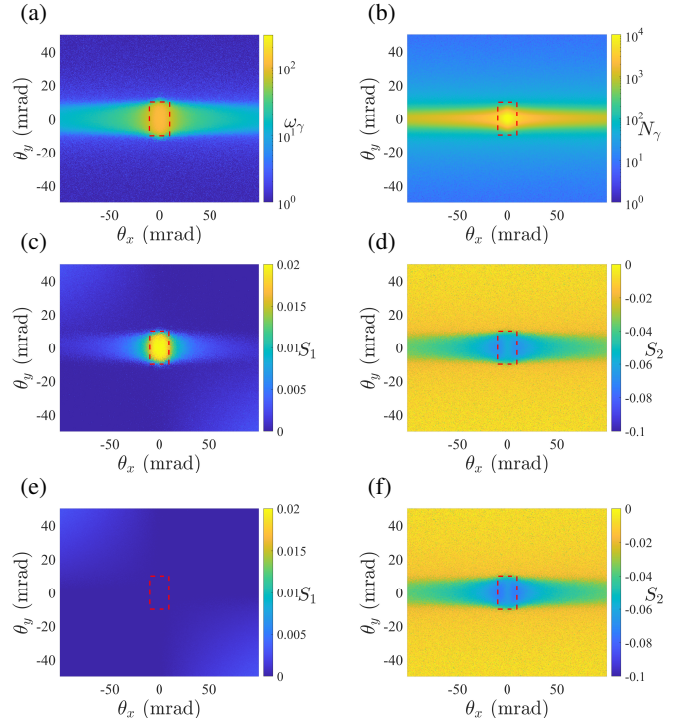


Figure 2: Angular distributions of (a) photon energy, (b) photon number, (c) Stokes parameter S_1 , and (d) S_2 from the full simulation including VP. Panels (e) and (f) show the corresponding S_1 and S_2 distributions when VP effects are artificially disabled. The dashed rectangle in all panels indicates the selection region applied to isolate high-energy photons for analysis, spanning ± 10 mrad in both horizontal and vertical divergence angles ($\theta_x, \theta_y \in [-10, 10]$ mrad).

Photons generated via nonlinear Compton scattering exhibit a strong forward peaking. As shown in Figure 2(a) and (b), both the mean photon energy and the photon flux are concentrated within a narrow cone of ~ 10 mrad half-angle. This behavior arises from two combined effects: first, electrons undergoing radiative energy loss emit higher-energy photons early in the

interaction, and these photons are scattered into smaller angles due to the large Lorentz factor of the beam ($\gamma_e \approx 6000$); second, in a linearly polarized laser field, the electron's transverse velocity is phase-shifted by $\pi/2$ relative to the electric field, resulting in negligible net transverse momentum and confining the radiation predominantly along the instantaneous electron velocity direction. Consequently, the central angular region contains both the highest photon energies and the majority of the photon yield.

Motivated by the fact that VB scales linearly with photon energy (via $\chi_\gamma \propto \omega_\gamma$), we restrict our analysis to photons within the rectangular region of ± 10 mrad in both transverse divergence angles (marked in all panels of Fig. 2). This selection retains over 85% of photons with energy above 1 GeV while discarding more than 90% of the low-energy background (~ 10 – 100 MeV). Within this region, the average photon energy is 107 MeV, and it contains 1.51×10^7 photons, of which 1×10^5 exceed 1 GeV. Experimentally, such a narrow angular cut can be conveniently implemented with a collimator placed on the beam axis, making this region both physically and diagnostically favorable.

The decisive signature of VB is revealed by comparing the angular distributions of the Stokes parameters S_1 and S_2 obtained with and without VP. In the absence of VP [Figure. 2(e) and (f)], the emitted photons are almost purely circularly polarized: S_1 remains negligible (average 0.00001) while S_2 exhibits a pronounced negative value (average -0.069), consistent with the helicity transfer from the longitudinally polarized electron beam [20]. When VP is included [Figure. 2(c) and (d)], a non-zero S_1 component emerges across the central angular region (average 0.019), directly reflecting the conversion of circular into linear polarization induced by the birefringent vacuum. The accompanying S_2 magnitude shows only a slight modification (average from -0.069 to -0.061), indicating that the VB-induced phase shift is still modest at the mean photon energy of the selected sample.

Although the average S_1 within the full selected region is only 0.019, this value is strongly weighted by the numerous sub-GeV photons, for which χ_γ is small and VB is weak. As we demonstrate in the next subsection, the substantial photon yield within the selected region effectively compensates for the modest average S_1 signal, providing a robust statistical foundation for the detection of vacuum birefringence.

3.2. Energy-Resolved VB Signature

To quantitatively assess the VB effect and its dependence on photon energy, we further analyse the selected photons by binning them in energy. Figure 3 plots the Stokes parameters S_1 , S_2 , S_3 , and the ratio S_1/S_2 as functions of photon energy ω_γ , comparing simulations with and without VP.

When VP is disabled (blue curves), S_1 remains essentially zero across the entire energy range, while $|S_2|$ approaches unity at high energies, see Figure. 3 (a) and (b), indicating strong circular polarization inherited from the longitudinally polarized electron beam. In stark contrast, when VP is active (red curves), a pronounced S_1 component appears for photons above $\omega_\gamma \gtrsim 0.5$ GeV, rising to ~ 0.45 at 2 GeV. This S_1 generation is accompanied by a substantial suppression of $|S_2|$, which drops

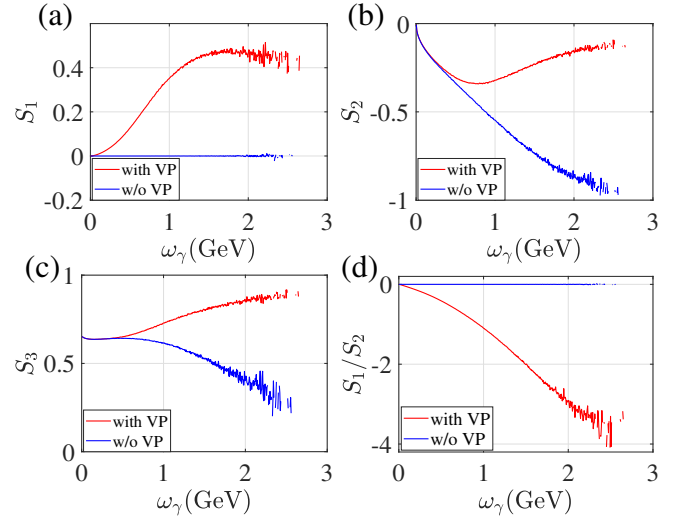


Figure 3: Signature of VB. Stokes parameters (a) S_1 , (b) S_2 , (c) S_3 , and (d) S_1/S_2 as functions of photon energy for photons within the angular selection region of Figure. 2. Red curves: results including VP (both VB and VD). Blue curves: results with VP artificially disabled.

from ≈ -0.9 to ≈ -0.15 over the same energy range. The simultaneous $S_2 \rightarrow S_1$ conversion and the reduction of circular polarization are the unambiguous hallmarks of VB.

The non-zero S_3 component visible in Figure. 3(c) (blue curve) is a well-known feature of nonlinear Compton scattering in a linearly polarized laser field [20]: it arises from the polarization-dependent emission probability and does not require vacuum effects. Additionally, Figure. 3(c) reveals a significant increase in S_3 at multi-GeV energies when VP is included. This effect arises from VD [27, 36, 37]: the polarization-dependent attenuation of photons due to nonlinear Breit–Wheeler pair production, which preferentially absorbs one helicity component and thereby modifies the ensemble-averaged Stokes vector.

The ratio S_1/S_2 , shown in Figure. 3(d), further emphasizes the growing influence of VB with photon energy. While the ratio remains near zero without VP, it reaches ~ -3 at 2 GeV when VP is included, directly quantifying the relative strength of the induced linear polarization compared to the residual circular component.

These energy-resolved results confirm that the VB signal is most pronounced for GeV-scale photons. Although such high-energy photons are less abundant than their sub-GeV counterparts, their large per-photon S_1 yield makes them the optimal carriers of the VB signature. The trade-off between signal strength and photon statistics is systematically addressed in the parameter optimization discussed in Sec. 4.

Figure 4(a) shows the buildup of linear polarization as a high-energy photon ($\omega_\gamma = 1.341$ GeV) traverses the laser pulse. The full simulation (red solid curve) exhibits a monotonic increase of S_1 , reaching ≈ 0.7 at the end of the interaction. This evolution is almost perfectly reproduced by the deterministic integration of the phase shift $\delta\phi$ derived from the polarization operator (blue dashed curve), confirming the accuracy of our Monte Carlo implementation.

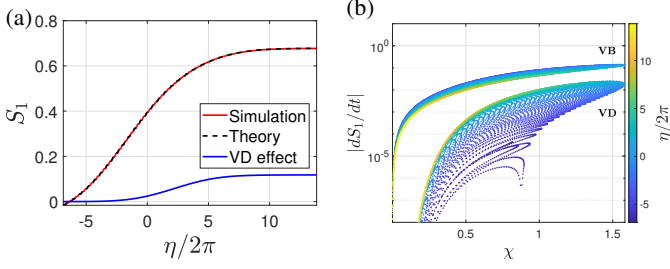


Figure 4: (a) Evolution of the Stokes parameter S_1 as a function of the laser phase $\eta = \omega_0 t - k_0 z$ for a 1 GeV photon. Red solid line: full Monte Carlo simulation including both VB and VD. Blue dashed line: deterministic integration of the VP-induced phase shift based on the nonperturbative polarization operator (Eqs. 11 and Eqs. 20). Blue solid line: contribution from VD alone, obtained by Eqs. 20. (b) Comparison of the instantaneous polarization rotation rates dS_1/dt arising from VB and VD as a function of the quantum parameter χ_γ for the same 1.341 GeV photon. The dots represent simulation data. The color gradient of the points reflects the evolution of the laser phase (interaction time).

In contrast, the contribution arising solely from VD (blue solid curve), computed by artificially disabling the VB-induced rotation, remains below 0.119 throughout the entire interaction. For this specific single-photon track, the integrated change due to VD is $(\Delta S_1, \Delta S_2, \Delta S_3) = (-0.118, 0.078, 0.361)$. We emphasize that these values represent the specific dynamical response of a single 1.341 GeV photon rather than an energy-averaged ensemble. Although VD is not negligible for GeV-scale photons, it is clearly subdominant; the vast majority of the S_1 signal originates from the coherent phase accumulation of VB.

To further resolve the local interaction dynamics, the instantaneous polarization change rates dS_1/dt arising from VB and VD are plotted against the quantum parameter χ_γ in Fig. 4(b) for the same 1.341 GeV photon track. Each point in the scatter plot represents a specific instant along the trajectory, with the color gradient encoding the evolution of the laser phase. The VB-induced rotation rate dominates the interaction, exhibiting a characteristic scaling consistent with the $\chi_\gamma^{2/3}$ dependence predicted by the local constant field approximation[26, 38, 39]. In contrast, the change rate due to VD remains significantly lower across the entire range of experienced χ_γ , even at the peak of the pulse. The clear separation between these two rates throughout the photon's path provides direct dynamical evidence that the observed S_1 signal is a primary manifestation of the dispersive vacuum ellipticity. This differential analysis reinforces the conclusion that the macroscopic polarization signal can be reliably attributed to VB.

4. Measurement Scheme and Parameter Optimization

To experimentally observe the VB signal, we adopt a polarimetry scheme based on the azimuthal distribution of electron-positron pairs produced when the γ -photons strike a high-Z converter (e.g., tungsten) [13]. The differential cross-section for pair production in the converter is given by:

$$d\sigma_{pp} = \frac{d\varphi}{2\pi} \{S_0\sigma_0 + [S_1 \sin(2\varphi) + S_3 \cos(2\varphi)]\sigma_1\}, \quad (21)$$

where φ is the azimuthal angle of the produced pairs, σ_0 and σ_1 are the unpolarized and polarized cross-section coefficients,

and S_i are the Stokes parameters of the photon beam. The linear polarization S_1 manifests as an azimuthal modulation, which can be extracted via the asymmetry parameter R_B :

$$R_B = \frac{(N_{\pi/4} + N_{5\pi/4}) - (N_{3\pi/4} + N_{7\pi/4})}{(N_{\pi/4} + N_{5\pi/4}) + (N_{3\pi/4} + N_{7\pi/4})}. \quad (22)$$

Here, N_φ represents the number of pairs falling into azimuthal bins centered at angle φ . For our broadband spectrum $n(\omega)$, the effective asymmetry $\langle R_B \rangle_{\text{eff}}$ is averaged over the photon energy:

$$\langle R_B \rangle_{\text{eff}} \approx \frac{\sin(2\beta)}{2\beta} \frac{\int d\omega n(\omega) \frac{\sigma_1(\omega)}{\sigma_0(\omega)} S_1(\omega)}{\int d\omega n(\omega) S_0(\omega)}, \quad (23)$$

where 2β is the azimuthal bin width. Based on our simulation, the generated average polarization $S_1 \approx 0.019$ translates to a measurable asymmetry $\langle R_B \rangle_{\text{eff}} \approx 1.48 \times 10^{-3}$.

The statistical significance of the detection is determined by the total number of accumulated photons N_γ . To reach an $n\sigma$ confidence level (e.g., 5σ), the required photon number must satisfy:

$$N_\gamma = \frac{\pi n_\sigma^2}{4\eta_{\text{eff}}\beta S_0 \langle R_B \rangle_{\text{eff}}^2}, \quad (24)$$

where η_{eff} is the effective pair-production conversion efficiency. Substituting our parameters into Eq. (24), the total photons required for a 5σ detection is $N_\gamma^{\text{req}} \approx 2.59 \times 10^9$. Further details could be found in Supplemental Material[40].

Since our baseline parameters ($a_0 = 125, E_e = 3$ GeV, and $N_e = 10^8$) yield $N_\gamma \approx 1.21 \times 10^9$ photons per shot, the required number of shots is:

$$N_{\text{shots}} = N_\gamma^{\text{req}}/N_\gamma^{\text{shot}} \approx 2. \quad (25)$$

This demonstrates that a 5σ detection is feasible in just two laser shots at near-future multi-petawatt facilities. This high-efficiency scheme overcomes the low repetition rate of high-power lasers, providing a robust pathway for the first definitive observation of VB.

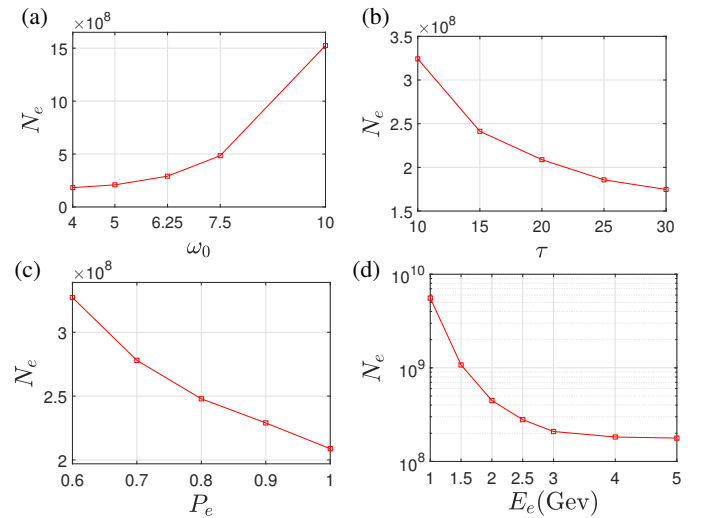


Figure 5: Required initial electron number N_e for a 5σ VB signal, plotted against (a) spot size w_0 , (b) pulse duration τ_p , (c) initial electron polarization, and (d) electron beam energy E_e .

Figure 5 shows the required N_e as a function of experimental parameters under the constraint of a fixed 560 J laser energy. In Figure 5(a), N_e increases with w_0 because enlarging the spot size dilutes the peak intensity a_0 . Since the VB rotation rate scales as $dS_1/dt \propto \chi_\gamma^{2/3}$, a lower a_0 leads to a drastically smaller S_1 signal, requiring more electrons. Conversely, Figure 5(b) shows that N_e decreases for longer pulse durations τ_p . With fixed laser energy ($a_0^2 \tau_p \approx \text{const}$), the accumulated signal scales as $S_1 \propto a_0^{2/3} \tau_p \propto a_0^{-4/3}$. Thus, reasonably lowering a_0 by stretching the pulse duration actually enhances the total signal by providing a much longer interaction time for the VB phase to accumulate, effectively reducing the required N_e . While the initial electron polarization has a positive effect on the required N_e [Figure 5(c)],

Regarding the electron beam, Fig. 5(c) confirms that increasing the initial electron polarization P_e effectively reduces the required N_e . For electron beam energy, Figure 5(d) shows a regime of diminishing returns. As E_e exceeds 3 GeV, the required N_e plateaus. This is a direct consequence of the pair-production cascades. As shown in Figure 6, while primary photons carrying the VB signal are absorbed at high E_e , the electron pairs generate a surge of secondary cascade photons. These unpolarized secondary photons dilute the ensemble-averaged S_1 , counteracting the benefits of higher beam energy.

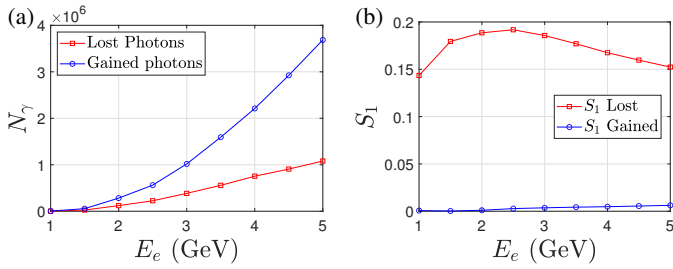


Figure 6: Comparison of lost photons (absorbed) and gained photons (generated by electron pairs) vs. E_e . The exponential surge in unpolarized cascade photons at high energy dilutes the ensemble-averaged S_1 signal, leading to the N_e plateau observed in Fig. 5(d).

Therefore, the optimal E_e must strike a balance: it must be high enough to ensure sufficient photon yield and χ_γ , but low enough to prevent signal dilution via pair-production cascades. Our results confirm that $a_0 \sim 125$ and $E_e \sim 3$ GeV offer this optimal window, maximizing the birefringent signature while isolating it from cascade contamination.

5. Conclusion

In conclusion, we have proposed and numerically demonstrated a compact scheme for observing VB. By integrating γ -photon generation and probing into a single laser-electron interaction, our approach avoids key limitations of conventional pump-probe setups. This unified architecture eliminates the demanding requirements for femtosecond-level synchronization and external beam transport optics inherent to multi-beam experiments. This guarantees a perfect spatiotemporal overlap and maximizes the accumulated phase shift, yielding a clear and robust signature: a generated linear polarization component

($S_1 \approx 0.019$ for angular selected photons) that is the direct evidence of the induced ellipticity within the birefringent quantum vacuum. We have identified an optimal operational window around $a_0 \sim 125$ and $E_e \sim 3$ GeV, where the coherent birefringent signal is maximized while reducing the competing influence of VD. This trade-off highlights the importance of managing signal quality over mere photon quantity. The high photon yield of nonlinear Compton-scattering, combined with an analysis that integrates polarization information over the entire emitted spectrum, makes a 5σ confidence-level detection feasible with as few as two laser shots at current multi-petawatt laser and accelerator facilities. This work therefore presents a robust and practical pathway toward a first definitive confirmation of VB. By enabling the simultaneous observation of both the dispersive (birefringence) and absorptive (dichroism) properties of the vacuum, this scheme opens up new path for experimentally studying the optical nature of the quantum vacuum in the strong-field limit.

References

- [1] G. V. Dunne, Heisenberg–euler effective lagrangians: basics and extensions, in: *From Fields to Strings: Circumnavigating Theoretical Physics: Ian Kogan Memorial Collection* (In 3 Volumes), World Scientific, 2005, pp. 445–522. doi:10.1142/5621.
- [2] W. Heisenberg, H. Euler, Folgerungen aus der diracschen theorie des positrons, *Zeitschrift für Physik (Journal of Physics)* 98 (1936) 714–732. doi:10.1007/BF01343663.
- [3] H. Euler, B. Kockel, Über die streuung von licht an licht nach der diracschen theorie, *Naturwissenschaften* 23 (15) (1935) 246–247.
- [4] G. Zavattini, F. Della Valle, A. Ejlli, G. Ruoso, A polarisation modulation scheme for measuring vacuum magnetic birefringence with static fields, *The European Physical Journal C* 76 (5) (2016) 294. doi:10.1140/epjc/s10052-016-4139-0.
- [5] A. Cadène, P. Berceau, M. Fouché, R. Battesti, C. Rizzo, Vacuum magnetic linear birefringence using pulsed fields: Status of the bmv experiment, *The European Physical Journal D* 68 (Feb. 2013). doi:10.1140/epjd/e2013-40725-9.
- [6] A. Ejlli, F. Della Valle, U. Gastaldi, G. Messineo, R. Pengo, G. Ruoso, G. Zavattini, The pvlas experiment: A 25 year effort to measure vacuum magnetic birefringence, *Physics Reports* 871 (2020) 1–74. doi:10.1016/j.physrep.2020.06.001.
- [7] H.-P. Schlenvoigt, T. Heinzl, U. Schramm, T. E. Cowan, R. Sauerbrey, Detecting vacuum birefringence with x-ray free electron lasers and high-power optical lasers: A feasibility study, *Physica Scripta* 91 (2) (2016) 023010. doi:10.1088/0031-8949/91/2/023010.

- [8] N. Ahmadinia, C. Bähz, A. Benediktovitch, C. Bömer, L. Bocklage, T. Cowan, J. Edwards, S. Evans, S. F. Viñas, H. Gies, et al., Towards a vacuum birefringence experiment at the helmholtz international beamline for extreme fields (letter of intent of the biref@ hibef collaboration), *High Power Laser Science and Engineering* 13 (2025) e7. doi: [10.1017/hpl.2024.70](https://doi.org/10.1017/hpl.2024.70).
- [9] E. A. Mosman, F. Karbstein, Vacuum birefringence and diffraction at an x-ray free-electron laser: From analytical estimates to optimal parameters, *Physical Review D* 104 (1) (2021) 013006. arXiv:2104.05103, doi: [10.1103/PhysRevD.104.013006](https://doi.org/10.1103/PhysRevD.104.013006).
- [10] F. Karbstein, C. Sundqvist, K. S. Schulze, I. Uschmann, H. Gies, G. G. Paulus, Vacuum birefringence at x-ray free-electron lasers, *New Journal of Physics* 23 (9) (2021) 095001. doi: [10.1088/1367-2630/ac1df4](https://doi.org/10.1088/1367-2630/ac1df4).
- [11] M. Formanek, J. P. Palastro, D. Ramsey, S. Weber, A. Di Piazza, Signatures of vacuum birefringence in low-power flying focus pulses, *Physical Review D* 109 (5) (2024) 056009. doi: [10.1103/PhysRevD.109.056009](https://doi.org/10.1103/PhysRevD.109.056009).
- [12] B. King, N. Elkina, Vacuum birefringence in high-energy laser-electron collisions, *Physical Review A* 94 (6) (2016) 062102. doi: [10.1103/PhysRevA.94.062102](https://doi.org/10.1103/PhysRevA.94.062102).
- [13] S. Bragin, S. Meuren, C. H. Keitel, A. Di Piazza, High-energy vacuum birefringence and dichroism in an ultra-strong laser field, *Physical Review Letters* 119 (25) (2017) 250403. doi: [10.1103/PhysRevLett.119.250403](https://doi.org/10.1103/PhysRevLett.119.250403).
- [14] Y. Nakamiya, K. Homma, Probing vacuum birefringence under a high-intensity laser field with gamma-ray polarimetry at the gev scale, *Physical Review D* 96 (5) (2017) 053002. doi: [10.1103/PhysRevD.96.053002](https://doi.org/10.1103/PhysRevD.96.053002).
- [15] C. Lv, F. Wan, Y. I. Salamin, Q. Zhao, M. Ababekri, R. Xu, J.-X. Li, Generation of high-brilliance polarized γ -rays via vacuum dichroism-assisted vacuum birefringence (Apr. 2024). arXiv:2401.14075.
- [16] T. N. Wistisen, U. I. Uggerhøj, Vacuum birefringence by compton backscattering through a strong field, *Physical Review D* 88 (5) (2013) 053009. doi: [10.1103/PhysRevD.88.053009](https://doi.org/10.1103/PhysRevD.88.053009).
- [17] R. Taverna, R. Turolla, F. Muleri, et al., Polarized x-rays from a magnetar, *Science* 378 (6620) (2022) 646–650. arXiv:2205.08898, doi: [10.1126/science.add0080](https://doi.org/10.1126/science.add0080).
- [18] R. Mignani, V. Testa, D. G. Caniulef, R. Taverna, R. Turolla, S. Zane, K. Wu, Evidence for vacuum birefringence from the first optical polarimetry measurement of the isolated neutron star rx j1856. 5- 3754, *Monthly Notices of the Royal Astronomical Society* (2016) stw2798.
- [19] J. D. Brandenburg, J. Seger, Z. Xu, W. Zha, Report on progress in physics: observation of the breit–wheeler process and vacuum birefringence in heavy-ion collisions, *Reports on Progress in Physics* 86 (8) (2023) 083901.
- [20] Y.-F. Li, R. Shaisultanov, Y.-Y. Chen, F. Wan, K. Z. Hatsagortsyan, C. H. Keitel, J.-X. Li, Polarized ultrashort brilliant multi-gev γ -rays via single-shot laser-electron interaction, *Physical Review Letters* 124 (1) (2020) 014801. arXiv:1907.08877, doi: [10.1103/PhysRevLett.124.014801](https://doi.org/10.1103/PhysRevLett.124.014801).
- [21] Y.-F. Li, R.-T. Guo, R. Shaisultanov, K. Z. Hatsagortsyan, J.-X. Li, Electron polarimetry with nonlinear compton scattering, *Physical Review Applied* 12 (1) (2019) 014047. doi: [10.1103/PhysRevApplied.12.014047](https://doi.org/10.1103/PhysRevApplied.12.014047).
- [22] K.-H. Zhuang, Y.-Y. Chen, Y.-F. Li, K. Z. Hatsagortsyan, C. H. Keitel, Laser-driven lepton polarization in the quantum radiation-dominated reflection regime, *Physical Review D* 108 (3) (2023) 033001. doi: [10.1103/PhysRevD.108.033001](https://doi.org/10.1103/PhysRevD.108.033001).
- [23] V. Ritus, Quantum effects of the interaction of elementary particles with an intense electromagnetic field, *J. Sov. Laser Res.;(United States)* 6 (5) (1985).
- [24] T. Podszus, A. Di Piazza, High-energy behavior of strong-field qed in an intense plane wave, *Physical Review D* 99 (7) (2019) 076004. doi: [10.1103/PhysRevD.99.076004](https://doi.org/10.1103/PhysRevD.99.076004).
- [25] V. N. Baier, V. M. Katkov, V. M. Strakhovenko, *Electromagnetic processes at high energies in oriented single crystals*, World Scientific, 1998.
- [26] A. Di Piazza, M. Tamburini, S. Meuren, C. Keitel, Improved local-constant-field approximation for strong-field qed codes, *Physical Review A* 99 (2) (2019) 022125. arXiv:1811.05834, doi: [10.1103/PhysRevA.99.022125](https://doi.org/10.1103/PhysRevA.99.022125).
- [27] X.-Z. Wu, Y.-F. Li, Y.-Y. Chen, Y.-T. Li, Achieving high polarization of photons emitted by unpolarized electrons in ultrastrong laser fields, *Communications Physics* 8 (1) (2025) 156. doi: [10.1038/s42005-025-02077-2](https://doi.org/10.1038/s42005-025-02077-2).
- [28] Y. I. Salamin, C. H. Keitel, Electron acceleration by a tightly focused laser beam, *Physical Review Letters* 88 (9) (2002) 095005. doi: [10.1103/PhysRevLett.88.095005](https://doi.org/10.1103/PhysRevLett.88.095005).
- [29] L. H. Thomas, The motion of the spinning electron, *Nature* 117 (2945) (1926) 514–514.
- [30] L. H. Thomas, I. the kinematics of an electron with an axis, *The London, Edinburgh, and Dublin Philosophical Magazine and Journal of Science* 3 (13) (1927) 1–22.

- [31] V. Bargmann, L. Michel, V. Telegdi, Precession of the polarization of particles moving in a homogeneous electromagnetic field, *Physical Review Letters* 2 (10) (1959) 435.
- [32] M. Walser, D. J. Urbach, K. Z. Hatsagortsyan, S. Hu, C. H. Keitel, Spin and radiation in intense laser fields, *Physical Review A* 65 (4) (2002) 043410.
- [33] Y.-N. Dai, K. Z. Hatsagortsyan, C. H. Keitel, Y.-Y. Chen, Fermionic signal of vacuum polarization in strong laser fields, *Physical Review D* 110 (1) (2024) 012008. doi: [10.1103/PhysRevD.110.012008](https://doi.org/10.1103/PhysRevD.110.012008).
- [34] A. Gonsalves, K. Nakamura, J. Daniels, C. Benedetti, C. Pieronek, T. De Raadt, S. Steinke, J. Bin, S. Bulanov, J. Van Tilborg, et al., Petawatt laser guiding and electron beam acceleration to 8 gev in a laser-heated capillary discharge waveguide, *Physical review letters* 122 (8) (2019) 084801.
- [35] K. Tanaka, K. Spohr, D. Balabanski, S. Balascuta, L. Capponi, M. Cernaianu, M. Cuciuc, A. Cucoanes, I. Dancus, A. Dhal, et al., Current status and highlights of the eli-np research program, *Matter and Radiation at Extremes* 5 (2) (2020).
- [36] Y.-F. Li, Y.-Y. Chen, W.-M. Wang, H.-S. Hu, Production of highly polarized positron beams via helicity transfer from polarized electrons in a strong laser field, *Physical Review Letters* 125 (4) (2020) 044802.
- [37] D. Y. Ivanov, G. Kotkin, V. Serbo, Complete description of polarization effects in e+ e-pair production by a photon in the field of a strong laser wave, *The European Physical Journal C-Particles and Fields* 40 (1) (2005) 27–40.
- [38] D. G. Sevostyanov, I. A. Aleksandrov, G. Plunien, V. M. Shabaev, Total yield of electron-positron pairs produced from vacuum in strong electromagnetic fields: Validity of the locally constant field approximation, *Physical Review D* 104 (7) (2021) 076014. doi: [10.1103/PhysRevD.104.076014](https://doi.org/10.1103/PhysRevD.104.076014).
- [39] I. A. Aleksandrov, V. M. Shabaev, Vacuum birefringence and dichroism in a strong plane-wave background (Mar. 2023). [arXiv:2303.16273](https://arxiv.org/abs/2303.16273).
- [40] See Supplemental Material, at [URL will be inserted by publisher] for the method of calculating the number of required electrons to achieve sufficient signal photons.

Supplemental Material for "Probing Vacuum Birefringence in an Ultrastrong Laser Field via High-energy Gamma-ray Polarimetry"

1. Statistical Significance and Confidence Level Evaluation

To thoroughly evaluate the feasibility of achieving a 5σ confidence-level detection in our setup, we present a detailed statistical derivation. We follow the formalism of Bragin *et al.* [1] for the polarization asymmetry and extend it to rigorously account for the broadband energy distribution of the probe photons in our experiment.

1.1. 1. Statistical framework for a monochromatic beam

In the polarimetry scheme, the observable is the asymmetry R_B defined from the azimuthal distribution of electron-positron pairs produced in a converter:

$$R_B = \frac{(N_{\pi/4} + N_{5\pi/4}) - (N_{3\pi/4} + N_{7\pi/4})}{(N_{\pi/4} + N_{5\pi/4}) + (N_{3\pi/4} + N_{7\pi/4})}. \quad (\text{S1})$$

For a quasi-monochromatic beam, the expectation value of R_B is given by [1]:

$$\langle R_B \rangle = \frac{\sin(2\beta)}{2\beta} \frac{\sigma_1}{\sigma_0} \frac{S_1}{S_0}, \quad (\text{S2})$$

where β is the half-width of the azimuthal bins, σ_0, σ_1 are the pair-production cross-section coefficients, and S_0, S_1 are the Stokes parameters of the photon beam.

The statistical uncertainty of R_B follows from error propagation applied to the multinomial distribution of the detected pairs. Assuming each photon produces a pair with probabilities p_A and p_B to fall into the two orthogonal azimuthal bins used for R_B , one obtains the standard deviation:

$$\langle (\Delta R_B)^2 \rangle = \frac{1 - \langle R_B \rangle^2}{N_\gamma (p_A + p_B)}. \quad (\text{S3})$$

In the weak-signal regime ($\langle R_B \rangle^2 \ll 1$), to claim a detection with a significance of n_σ standard deviations ($\langle R_B \rangle = n_\sigma \Delta R_B$), the required number of photons N_γ is:

$$N_\gamma = \frac{n_\sigma^2}{\langle R_B \rangle^2 (p_A + p_B)}. \quad (\text{S4})$$

By integrating the differential cross section over the azimuthal intervals of width 2β , one finds $p_A + p_B = \frac{4\beta}{\pi} \eta S_0$, where $\eta = n_z l \sigma_0$ is the conversion efficiency. Equation (S4) then becomes:

$$N_\gamma = \frac{\pi n_\sigma^2}{4\eta\beta S_0 \langle R_B \rangle^2}. \quad (\text{S5})$$

1.2. 2. Extension to a broadband photon spectrum

In our setup, the probe photons exhibit a broad energy spectrum $n(\omega)$ (see Fig. S1(a)). Consequently, both the Stokes parameters and the cross-section ratio σ_1/σ_0 depend on photon energy. The effective asymmetry must be averaged over the spectrum:

$$\langle R_B \rangle_{\text{eff}} = \frac{\sin 2\beta}{2\beta} \frac{\int d\omega n(\omega) \frac{\sigma_1(\omega)}{\sigma_0(\omega)} S_1(\omega)}{\int d\omega n(\omega) S_0(\omega)}. \quad (\text{S6})$$

For our baseline parameters, the initial beam has $S_1 \approx 0$, and vacuum birefringence generates a small S_1 component. From our simulation (discarding photons below 1.02 MeV), we obtain the energy-resolved Stokes parameter $S_1(\omega)$ and the photon spectrum $n(\omega)$. The cross-sections $\sigma_0(\omega)$ for a tungsten converter ($Z = 74$) are extracted from the Hubbell [2] and are shown in Fig. S1(b).

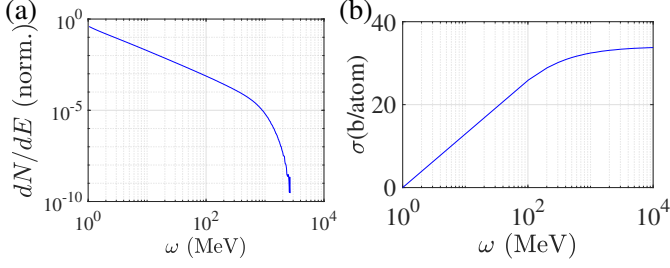


Figure S1: (a) Simulated photon energy spectrum $n(\omega)$ and corresponding $S_1(\omega)$. (b) Photon pair production cross sections $\sigma_0(\omega)$ on a Tungsten (W) target.

Performing the numerical integration yields:

$$\langle R_B \rangle_{\text{eff}} \approx 1.481 \times 10^{-3}. \quad (\text{S7})$$

This value is rigorously consistent with the energy-averaged Stokes parameter and the approximate monochromatic cross-section ratio once the spectral weights are taken into account.

The effective conversion efficiency also requires spectral averaging:

$$\eta_{\text{eff}} = n_z l \frac{\int d\omega n(\omega) \sigma_0(\omega)}{\int d\omega n(\omega)} = n_z l \langle \sigma_0 \rangle. \quad (\text{S8})$$

By integrating the pair-production cross-sections over our specific photon spectrum for a chosen 10 mRL Tungsten converter thickness, the effective conversion efficiency is calculated to be $\eta_{\text{eff}} \approx 6.005 \times 10^{-3}$. Substituting $\langle R_B \rangle_{\text{eff}} = 1.481 \times 10^{-3}$, $\eta_{\text{eff}} = 6.005 \times 10^{-3}$, $\beta = 33^\circ$ (i.e., 0.576 rad), $S_0 \approx 1$, and $n_\sigma = 5$ into Eq. (S5) gives:

$$N_\gamma^{\text{req}} = \frac{\pi \times 5^2}{4 \times 6.005 \times 10^{-3} \times 0.576 \times 1 \times (1.481 \times 10^{-3})^2} \approx 2.587 \times 10^9. \quad (\text{S9})$$

With a per-shot photon yield of $N_\gamma^{\text{shot}} \approx 1.21 \times 10^9$ (for $N_e = 10^8$ initial electrons), the number of required shots is:

$$N_{\text{shots}} = \frac{N_\gamma^{\text{req}}}{N_\gamma^{\text{shot}}} \approx 2. \quad (\text{S10})$$

This demonstrates that the broadband high-flux scheme can achieve a 5σ confidence level in just a few shots.

2. Experimental Setup and Detection Strategy

2.1. Signal Optimization via Energy Selection (Optional)

While the baseline analysis in the main text demonstrates that a 5σ significance can be readily achieved

by integrating over the generated broadband spectrum, the statistical weight of the vacuum birefringence signal is not uniformly distributed across all energies. Based on Eq. (S5), the required statistics scale as $N_\gamma \propto S_1^{-2} \sigma^{-1}$. To identify the most efficient energy range, we define a statistical sensitivity metric $S \propto N_\gamma S_1^2 \sigma$, which directly determines the confidence level of the signal.

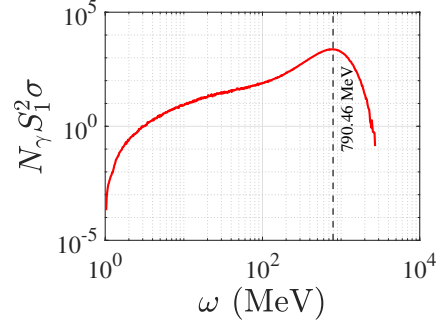


Figure S2: Statistical sensitivity metric $N_\gamma S_1^2 \sigma$ as a function of photon energy ω_γ . The metric reaches its maximum near ~ 790 MeV.

As shown in Fig. S2, this sensitivity metric is negligible below 100 MeV but peaks strongly around $\omega_\gamma \approx 790$ MeV. Therefore, an optional but highly effective experimental strategy to mitigate the high flux of sub-GeV background photons—which might otherwise saturate sensitive detectors—is to employ a magnetic spectrometer immediately after the conversion target.

It is crucial to note that the magnetic field acts on charged particles, not the photons themselves. By tuning the spectrometer to selectively deflect the e^+e^- pairs generated by photons in the 750 – 850 MeV window, one can spatially separate the high-value signal pairs from the dense, straight-line background of unconverted low-energy photons and broadly dispersed low-energy pairs. This spatial separation directs only the kinematically selected signal pairs onto the Image Plates, thereby significantly optimizing the experimental signal-to-noise ratio without distorting the intrinsic azimuthal polarization signature.

2.2. Beam Parameters and Pointing Stability

A vital aspect of experimental feasibility is the stability and physical size of the electron beam relative to the laser focal spot. We conservatively adopt an electron beam size of $\sigma_e = 2 \mu\text{m}$. Because the

electrons are distributed across the nonparaxial Gaussian profile of the laser ($w_0 = 5 \mu\text{m}$), the ensemble-averaged quantum parameter χ is slightly lower than for an ideal point-like beam. However, this geometric reduction is easily compensated by a modest increase in the total electron bunch charge (to $N_e \approx 2.247 \times 10^8$, corresponding to a highly feasible 5% influence).

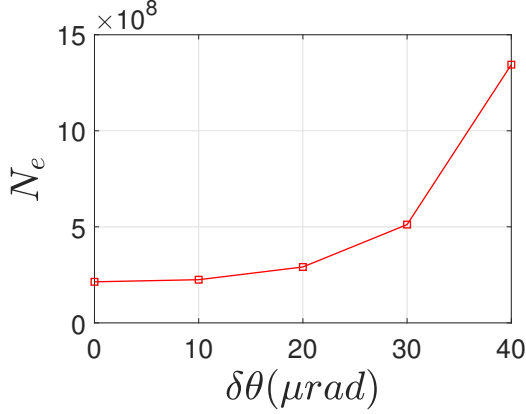


Figure S3: Number of initial electrons N_e required for a 5σ significance detection under varying angular beam jitter conditions.

Furthermore, the setup is highly robust against typical spatial jitter. For an interaction distance of 10 cm, a realistic angular jitter of $\delta\theta = 30 \mu\text{rad}$ results in a $3 \mu\text{m}$ transverse displacement at the focus. Since the laser waist $w_0 = 5 \mu\text{m}$ remains larger than both the beam size and the jitter displacement, the interaction reliably occurs within the high-intensity core of the laser pulse. As shown in Fig. S3, even with increasing jitter, the required number of electrons to maintain a 5σ significance remains well within the capabilities of current conventional accelerator facilities.

2.3. Background and Systematic Uncertainties

Residual Gas Background: Under typical high-vacuum conditions ($< 10^{-6}$ Torr) within the interaction chamber, the background gamma-ray yield originating from electron bremsstrahlung with residual gas molecules is estimated to be multiple orders of magnitude lower than the signal generated via nonlinear Compton scattering. Furthermore, bremsstrahlung photons are predominantly concentrated in the very low-energy regime, posing a negligible impact on the detection of the GeV-scale polarization signatures.

Multiple Coulomb Scattering (MCS): The linear polarization of the incident photons (S_1) is determined by observing the 'X-shaped' azimuthal distribution of the e^+e^- pairs. A primary physical source of systematic uncertainty is the blurring of this spatial distribution due to MCS as pairs exit the converter foil. For ~ 400 MeV electrons/positrons traversing a 10 mRL Tungsten target ($\sim 35 \mu\text{m}$), the RMS scattering angle is calculated as [3]:

$$\theta_0 = \frac{13.6 \text{ MeV}}{\beta c p} z \sqrt{x/X_0} [1 + 0.038 \ln(x/X_0)] \approx 3 \text{ mrad}. \quad (\text{S11})$$

Given that the intensity profile is typically recorded at a characteristic polar angle (beam spot size) of $\theta_{\text{obs}} \approx 10$ mrad, the effective azimuthal resolution is $\sigma_\phi \approx \theta_0/\theta_{\text{obs}} \approx 0.3$. Based on the angular dilution model [4], this results in a dilution factor $D = \exp(-2\sigma_\phi^2) \approx 0.84$. This means approximately 84% of the intrinsic polarization signal is preserved. Because the scattering-induced angular migration (~ 3 mrad) is significantly smaller than the macroscopic azimuthal span of the X-shape quadrants, the structural integrity of the polarization signature remains robust against MCS blurring.

Instrumental Asymmetries: Finally, instrumental defects such as magnetic field inhomogeneities or detector misalignments could potentially induce a 'fake' azimuthal modulation. However, in modern experimental setups, detector relative alignments can be routinely maintained to a precision better than 1 mrad [5]. Any geometric distortion from the apparatus is therefore sub-dominant compared to the physical scattering scale ($\theta_0 \approx 3$ mrad), ensuring that the observed excess of particle density in the diagonal quadrants is a genuine QED effect of the photon polarization state rather than an artifact of experimental bias.

References

- [1] S. Bragin, S. Meuren, C. H. Keitel, A. Di Piazza, High-energy vacuum birefringence and dichroism in an ultrastrong laser field, *Physical Review Letters* 119 (25) (2017) 250403. doi: [10.1103/PhysRevLett.119.250403](https://doi.org/10.1103/PhysRevLett.119.250403).
- [2] J. H. Hubbell, H. A. Gimm, I. O'verbo/, Pair, triplet, and total atomic cross sections (and mass

attenuation coefficients) for 1 mev-100 gev photons in elements $z = 1$ to 100, Journal of Physical and Chemical Reference Data 9 (4) (1980) 1023–1148. [doi:10.1063/1.555629](https://doi.org/10.1063/1.555629).

- [3] D. E. Groom, S. Klein, Passage of particles through matter: In review of particle physics (rpp 2000), The European Physical Journal C 15 (1-4) (2000) 163–173. [doi:10.1007/BF02683419](https://doi.org/10.1007/BF02683419).
- [4] D. Bernard, Polarimetry of cosmic gamma-ray sources above e+e- pair creation threshold, Nuclear Instruments and Methods in Physics Research Section A: Accelerators, Spectrometers, Detectors and Associated Equipment 729 (2013) 765–780. [arXiv:1307.3892](https://arxiv.org/abs/1307.3892), [doi:10.1016/j.nima.2013.07.047](https://doi.org/10.1016/j.nima.2013.07.047).
- [5] J. Alcorn, B. Anderson, K. Aniol, et al., Basic instrumentation for hall a at jefferson lab, Nuclear Instruments and Methods in Physics Research Section A: Accelerators, Spectrometers, Detectors and Associated Equipment 522 (3) (2004) 294–346. [doi:10.1016/j.nima.2003.11.415](https://doi.org/10.1016/j.nima.2003.11.415).
- [6] I. Aleksandrov, V. Shabaev, Vacuum birefringence and dichroism in a strong plane-wave background, Zhurnal Eksperimentalnoi i Teoreticheskoi Fiziki (Journal of Experimental and Theoretical Physics) 166 (2) (2024) 182–193. [doi:10.31857/S0044451024080042](https://doi.org/10.31857/S0044451024080042).
- [7] V. Dinu, T. Heinzl, A. Ilderton, M. Marklund, G. Torgrimsson, Vacuum refractive indices and helicity flip in strong-field qed, Physical Review D 89 (12) (2014) 125003. [doi:10.1103/PhysRevD.89.125003](https://doi.org/10.1103/PhysRevD.89.125003).